Nanoscale Research Letters

NANO EXPRESS Open Access

# Fabrication of CdTe QDs/BiOI-Promoted $TiO_2$ Hollow Microspheres with Superior Photocatalytic Performance Under Simulated Sunlight

Xiaofei Qu[1], Meihua Liu[1], Longfei Li[1], Chunqi Wang[1], Cuihua Zeng[1], Jianhuang Liu[2], Liang Shi[1*] and Fanglin Du[1]

## Abstract

Hollow and heterostructured architectures are recognized as an effective approach to improve photocatalytic performance. In this work, ternary $TiO_2$/CdTe/BiOI with hollow structure was constructed via a step-by-step method. In addition, the effect of $TiO_2$ structural regulation and the energy band alignment of BiOI and CdTe quantum dots (CdTe QDs) with $TiO_2$ in $TiO_2$/CdTe/BiOI on photocatalytic dye removal were also studied. The results reveal that the $TiO_2$/CdTe/BiOI heterostructures with hollow substrates exhibit much higher photocatalytic activities than pure $TiO_2$, P25, $TiO_2$/CdTe, and $TiO_2$/BiOI and ternary $TiO_2$/CdTe/BiOI with solid substrates. For $TiO_2$(H)/CdTe/BiOI, several synergistic factors may be responsible for the remarkable visible-light photodegradation performance, such as strong visible-light absorption by BiOI and larger specific surface area.

**Keywords:** Photocatalysis, Ternary heterojunctions, CdTe quantum dots, $TiO_2$ hollow microspheres

## Background

Owing to the energy saving and environmentally friendly merits, semiconductor photocatalysis has drawn increasing interests in environmental conservation. Photocatalysts can be used in various aspects, such as self-cleaning, water treatment, air purification, and anti-bacteria [1, 2]. Among them, due to the advantages of low cost, excellent stability, and nontoxicity [3], titanium dioxide ($TiO_2$) has been extensively investigated. However, it can only utilize small portion of solar spectrum because of its wide bandgap and relatively rapid charge recombination, limiting the photo-conversion efficiency [4].

In order to improve the visible-light photocatalytic efficiency of titania, various strategies have been adopted including ion doping, noble metal loading, heterojunction constructing, and sensitization [5–8]. Among these strategies, heterojunction formed by coupling with narrow bandgap semiconductor is supposed to be one of the most effective methods to improve the visible-light response and reduce charge recombination simultaneously [9].

Bismuth oxyhalides have attracted considerable attention due to low cost, good stability, and wide light-response range [10, 11], which have an isotropic-layered structure with $[Bi_2O_2]^{2+}$ layers intercalated by $X^-$ ions (X = F, Cl, Br, I) [12]. Among the bismuth oxyhalides, BiOI with the smallest bandgap (1.72–1.9 eV) [13] has been proven to be an efficient visible-light photocatalyst for the degradation of RhB [14] and MO [15]. The internal electric field between the $[Bi_2O_2]^{2+}$ and $I^-$ layers can promote the separation of photo-induced charges and enhance the photocatalytic activity [16]. Although both the conduction band and valence band potentials lie between those of $TiO_2$, type II heterojunction could be formed by coupling p-type BiOI and n-type $TiO_2$ together when Fermi levels reach equilibrium, thus making conduction band electrons of BiOI migrate to $TiO_2$ [17]. Up to now, although many efforts have been devoted to develop binary heterostructured photocatalysts, the limited visible-light response and relatively low charge separation efficiency are still the stumbling block.

To solve the issues mentioned above, multi-component heterojunction systems have been developed. Cadmium

* Correspondence: shiliang@qust.edu.cn
[1]College of Materials Science and Engineering, Qingdao University of Science and Technology, Zhengzhou Road 53, Qingdao 266042, China
Full list of author information is available at the end of the article

telluride (CdTe), as an important p-type II–VI compound semiconductor, has received much attention because of its direct bandgap of 1.44 eV [18] and a large optical absorption coefficient in the solar spectrum [19]. CdTe quantum dots (CdTe QDs) have been widely used to modify various semiconductors: Feng et al. [20] synthesized the CdTe-decorated $TiO_2$ nanotube arrays via a pulse electrodeposition method, and the results indicated CdTe/$TiO_2$ nanotube arrays (CdTe/$TiO_2$ NTAs) exhibited outstanding photocatalytic property than the bare $TiO_2$ NTAs; Liu et al. [21] reported the synthesis of CdTe/ZnO nanocomposites by a hot bath method, and the results showed that CdTe/ZnO owed a better photocatalytic activity for Rhodamine B than bare ZnO. However, apart from binary heterostructured photocatalysts, ternary-heterostructured $TiO_2$/BiOI modified with CdTe QDs may present fascinating photocatalytic performance and be worthy of being studied further.

In the present work, CdTe QDs/BiOI-modified $TiO_2$ was prepared for the photocatalytic application by a two-step method, and solid and hollow $TiO_2$ microspheres were applied as precursors. In addition, the structural evolution of $TiO_2$/CdTe/BiOI composites and the synergetic effect of CdTe and BiOI in photocatalytic process were also studied in detail.

## Methods

### Materials

Titanium isopropoxide (TTIP, 97%) and bismuth nitrate pentahydrate (AR, 99.0%) were purchased from Macklin Inc. Cadmium chloride hemi-pentahydrate ($CdCl_2{\cdot}2.5H_2O$, 99.0%), sodium tellurite ($Na_2TeO_3$, 98.0%), *N*-acetyl-*L*-cysteine (98.0%), potassium borohydride ($KBH_4$, 97%), sodium hydroxide (NaOH, 96.0%), potassium nitrate ($KNO_3$, 99%), potassium bromide (KBr, 99%), hydrochloric acid (HCl, 36–38%), hydrogen peroxide ($H_2O_2$, 30%), ethylene glycol, and absolute ethanol were all analytical grade and purchased from Sinopharm Chemical Reagent Co., Ltd.

### Synthesis of $TiO_2$ Solid Microspheres and Hollow Microspheres

In a typical procedure, 0.8 mL of $KNO_3$ solution (0.1 mol/L) was dissolved into 200 mL of ethanol. Then, 4.4 mL of TTIP was added to the above solution and stirred until white precipitate was generated. Aged for 12 h, the obtained white suspension was centrifuged and washed with deionized water and ethanol for several times, and the amorphous $TiO_2$ ($TiO_2{\cdot}nH_2O$) could be obtained. After being further dried at 60 °C for 12 h and calcined at 450 °C for 2 h, $TiO_2$ solid microspheres ($TiO_2$(S)) could be gained.

As for $TiO_2$ hollow microspheres, they were fabricated via a hydrothermal process. Typically, $TiO_2{\cdot}nH_2O$ (200 mg) were dispersed into 40 mL of 0.05 wt% $H_2O_2$ and stirred for 10 min. Then, 480 mg of NaOH powders was dissolved into the suspension above, and the mixture was transferred into a Teflon-lined autoclave and was kept at 180 °C for 4 h. The precipitates were collected and then were immersed in hydrochloride acid (0.1 mol/L). After being washed with deionized water several times, the resultants were dried and calcined as the previous procedure, and thus, $TiO_2$ hollow microspheres, labeled as $TiO_2$(H), were obtained.

### Synthesis of $TiO_2$ Spheres Modified with CdTe QDs

$TiO_2$ powders (2.0 g) were dispersed in 40 mL of deionized water, and then, 97.9 mg of *N*-acetyl-*L*-cysteine, 114.2 mg of $CdCl_2{\cdot}2.5H_2O$, and 178 mg of $KBH_4$ were subsequently added into the mixture at 30 min intervals. Afterwards, 10 mL $Na_2TeO_3$ (0.01 mol/L) aqueous solution was added into the above mixture with 5 mL/min. Then, the temperature of the system was elevated to 100 °C in 30 min and refluxed for 6 h. Finally, the products were washed with water and ethyl alcohol several times and dried at 60 °C for 12 h, and the products were labeled as $TiO_2$/CdTe.

### Fabrication of $TiO_2$/CdTe/BiOI Ternary Composites

Briefly, $TiO_2$/CdTe powders (258 mg) obtained above were dispersed in 10 mL of EG, forming a white suspension. Afterwards, a $Bi(NO_3)_3$ solution prepared by dissolving 627.6 mg of $Bi(NO_3)_3$ in 28 mL of EG was dropped into the above suspension in 15 min. Then, a solution containing 214.8 mg of KI and 24 mL of EG was dropped into the previous mixture. After stirring for 1 h, a yellow solution was transferred into the Teflon-lined autoclave and was kept at 80 °C for 3 h. The resulting precipitates were collected, sufficiently washed with ethanol and deionized water, and dried, which were labeled as $TiO_2$/CdTe/BiOI.

Binary $TiO_2$/BiOI heterostructures were obtained via the similar procedure by adding single component $TiO_2$ in the solution above.

### Characterization

X-ray diffraction (XRD) patterns were obtained on a Rigaku D-MAX2500 X-ray diffractometer fitted with Cu Kα radiation. Scanning electron microscopy (SEM) was obtained using JSM-6700F field emission scanning electron microscope (JEOL, Japan). Transmission electron microscopy (TEM) images of the samples were obtained on a JEM-2100 microscope (JEOL, Japan) at an accelerating voltage of 200 kV. Nitrogen adsorption/desorption isotherms were measured at 77 K using a surface area and pore size analyzer (NOVA 1000e, Quantachrome Instruments), and the Brunauer-Emmett-Teller (BET) method was applied to evaluate the specific surface area. X-ray photoelectron spectroscopy (XPS) analysis was performed

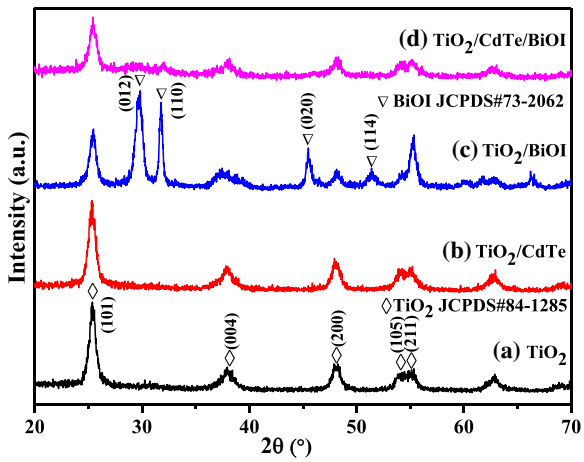


**Fig. 1** XRD patterns of **a** bare $TiO_2$, **b** $TiO_2$/CdTe, **c** $TiO_2$/BiOI, and **d** $TiO_2$/CdTe/BiOI

on an XSAM800 (Kratos Corporation, UK) with an Al Kα (1486.6 eV) achromatic X-ray source. The optical absorption spectra and diffuse reflection spectra (DRS) were obtained using an ultraviolet-visible spectrophotometer (CARY500UV, Varian). Photoluminescence spectra were recorded using Shimadzu RF-5301 with an excitation wavelength of 365 nm. Transient photocurrent was analyzed by an electrochemical workstation (CHI760E, Shanghai Chenhua, China) with a standard three-electrode system which used catalyst-deposited FTO glass as working electrode, Pt as the counter electrode, and SCE as the reference electrode in the electrolyte of 0.5 M $Na_2SO_4$.

### Photocatalytic Performance

Photocatalytic activity of the synthesized composites was tested based on the degradation of methyl orange (MO), using 500 W Xe-arc lamp as light source. Here, an amount of 140 mg of photocatalysts was added to 50 mL of MO solution (5 mg/L) taken in a quartz beaker. Prior to illumination, the suspension was stirred for 30 min in a dark chamber to achieve adsorption-desorption equilibrium between photocatalysts and MO solution. The mixture was then irradiated for 180 min, and 4 mL aliquot of solution was sampled at every 45 min intervals. The mixture was centrifuged at 8000 rpm for 3 min in order to remove the catalysts from the supernatant. In the stability test of photocatalyst, the samples were washed with deionized water after each cycle and then added to a fresh MO solution for the next cycle. The residual concentration of MO was monitored using a UV-vis spectrophotometer (CARY500UV, Varian), and the degradation percentage was quantitatively analyzed by comparing the maximum absorption at 465 nm.

Generally, holes ($h^+$), electrons ($e^-$), superoxide radicals ($\bullet O^-_2$), and hydroxyl radicals (•OH) could be produced in the semiconductor photocatalytic system under irradiation. A radical scavenging test for the photo-induced active species was carried out. The scavenging experiment was similar to the photocatalytic decomposition tests, where

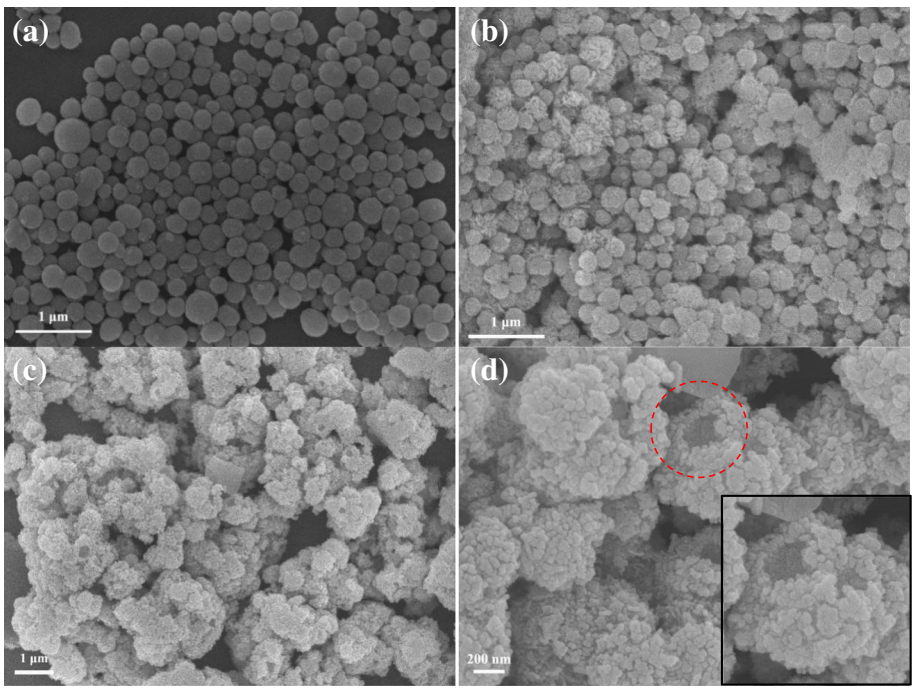


**Fig. 2** SEM images of **a** $TiO_2$(S)/CdTe, **b** $TiO_2$(S)/CdTe/BiOI, and **c**–**d** $TiO_2$(H)/CdTe/BiOI

ethylenediaminetetraacetic acid disodium salt (EDTA-2Na, 2 mmol/L), potassium bromate ($KBrO_3$, 10 mmol/L), benzoquinone (BQ, 1 mmol/L), and isopropyl alcohol (IPA, 10 mmol/L) were used for scavenging the $h^+$, $e^-$, $\bullet O^-_2$, and •OH reactive species, respectively.

## Results and Discussions

Figure 1 presents the powder X-ray diffraction patterns of $TiO_2$, $TiO_2$/CdTe, $TiO_2$/BiOI, and $TiO_2$/CdTe/BiOI. It is noted that $TiO_2$ characteristic peaks could be picked out in all the samples, and the peaks with 2θ values at 25.5°, 37.8°, 48.8°, 53.5°, and 55.6° can be indexed to (101), (004), (200) and (105), (211) facets of anatase (JCPDS #84-1285) [22]. From the patterns shown in Fig. 1c, d, the diffraction peaks at 2θ of 29.7°, 31.7°, 45.5°, and 51.3° are exhibited besides the peaks of $TiO_2$, which is consistent with tetragonal BiOI (JCPDS #73-2062) [23]. However, the peaks of BiOI are much more evident in $TiO_2$/BiOI than those of $TiO_2$/CdTe/BiOI. As for $TiO_2$/CdTe (Fig. 1b), no other peaks are found clearly in the XRD pattern besides $TiO_2$, because of the small crystallite size or a tiny amount dosage of CdTe QDs.

The external morphology of binary $TiO_2$/CdTe and ternary $TiO_2$/CdTe/BiOI is characterized using SEM, as displayed in Fig. 2. The overall observation of all the $TiO_2$-based composites exhibits a spherical morphology, with a diameter about 200-400 nm, and flake-like BiOI deposited on the surface of $TiO_2$ spheres except $TiO_2$/CdTe shown in Fig. 2a. The SEM image of $TiO_2$(S)/

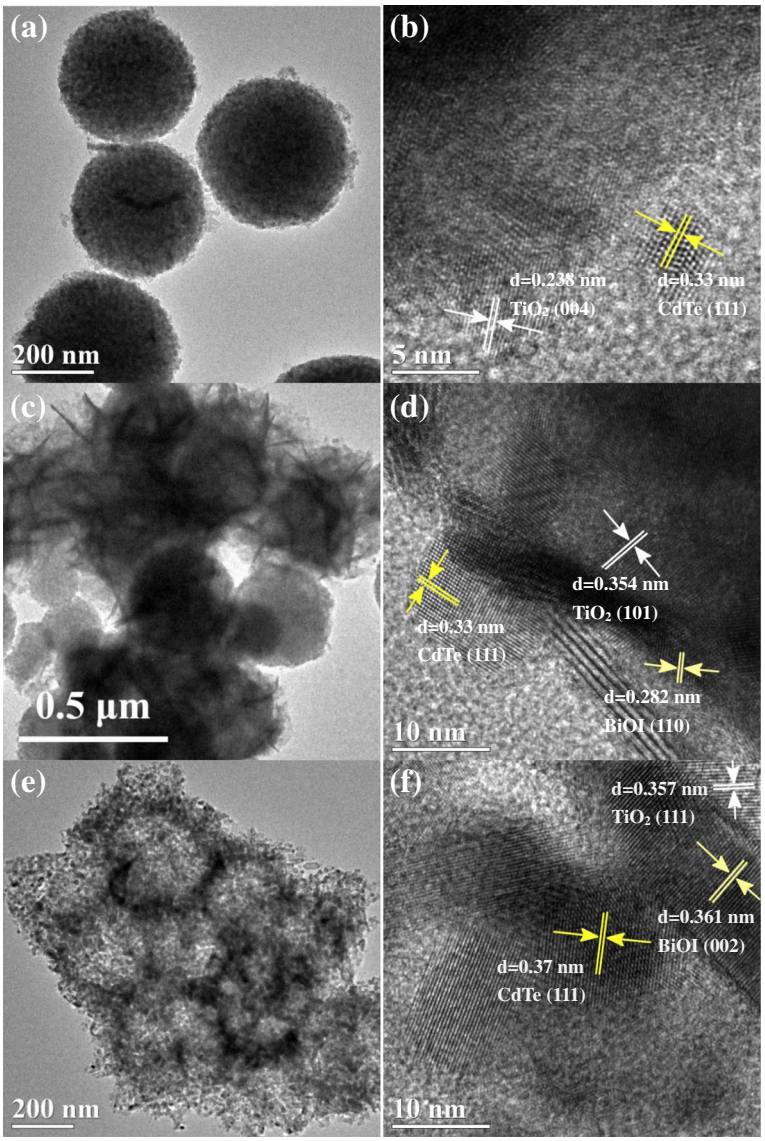


**Fig. 3** TEM images of **a**–**b** $TiO_2$(S)/CdTe, **c**–**d** $TiO_2$(S)/CdTe/BiOI, and **e**–**f** $TiO_2$(H)/CdTe/BiOI

CdTe/BiOI displayed in Fig. 2b shows a similar situation as $TiO_2$(S)/CdTe, and the $TiO_2$(S) spheres are covered by plenty of BiOI flakes with relatively regular morphologies. However, the case is quite different for $TiO_2$(H)/CdTe/BiOI, in which the particles possess nonuniform morphology with various size and cauliflower-like surface, as shown in Fig. 2c, d. Moreover, the BiOI flakes seem to be easier to attach on $TiO_2$(H)/CdTe caused by rough surface originated from $TiO_2$(H), and the pristine hollow structure of $TiO_2$(H) matrix could be identified in the magnified view.

TEM images give further insight into the structural evolution of the ternary $TiO_2$/CdTe/BiOI, as shown in Fig. 3. Uniform-sized and well-dispersed solid spherical $TiO_2$ can be clearly observed in Fig. 3a, and some tiny particles are also found in the region. Lattice spacing of 0.238 nm and 0.33 nm corresponding to the (004) plane of $TiO_2$ and the (111) plane of CdTe can be identified in Fig. 3b, demonstrating formation of heterojunctions between $TiO_2$ spheres and CdTe QDs. It can be seen from Fig. 3c that numerous flakes were attached to the surface of solid spherical $TiO_2$, and the lattice fringe was 0.282 nm in Fig. 3d, which is in accordance with the [110] direction of BiOI crystal. Moreover, the magnification of the interface also testifies the existence of CdTe QDs and BiOI flakes in $TiO_2$(S)/CdTe/BiOI. In contrast, Fig. 3e exhibits the $TiO_2$(H)/CdTe/BiOI which appears in the morphology of aggregated hollow spheres without apparent flake-like grains attached. The phenomenon implies BiOI components probably consist in much more smaller particles as the huge surface of $TiO_2$(H) spheres, which is composed by plenty of primary $TiO_2$ nanoparticles, decentralizes the nucleation sites. Similarly, the magnified view of the interface confirms the presence of heterostructured ternary $TiO_2$(H)/CdTe/BiOI composites, as shown in Fig. 3f, and the (111) crystal plane of CdTe and (002) of BiOI can be found clearly.

Figure 4 shows the nitrogen adsorption/desorption isotherms of the ternary $TiO_2$(S)/CdTe/BiOI and $TiO_2$(H)/CdTe/BiOI heterostructures. Both the isotherms exhibit similar characteristics of a type IV isotherm, according to the classification of IUPAC [24]. However, the $TiO_2$(S)/CdTe/BiOI possesses a H2 type hysteresis loop in the range 0.4-0.8 [25], which indicates the accumulation of uniform $TiO_2$ grains by direct calcination, while $TiO_2$(H)/CdTe/BiOI with a H3 type hysteresis loop due to staking pores is derived from hydrothermal nanosheets or nanotube precursors [10], and the results are in accordance with SEM and TEM images. In addition, the specific surface area of $TiO_2$(S)/CdTe/BiOI and $TiO_2$(H)/CdTe/BiOI was calculated to be 77.7 and 91.6 $m^2$ $g^{-1}$ using the Brunauer-Emmett-Teller (BET) method. A relatively larger surface area of

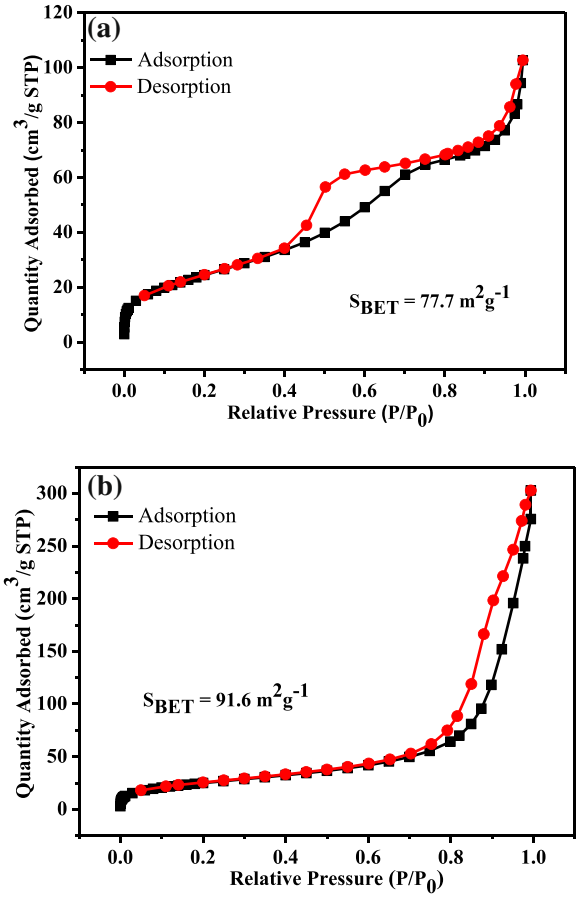


**Fig. 4** Nitrogen absorption-desorption isotherms of **a** $TiO_2$(S)/CdTe/BiOI and **b** $TiO_2$(H)/CdTe/BiOI

$TiO_2$(H)/CdTe/BiOI microspheres could provide more active sites for the adsorption of reactant molecules, resulting a more efficient photocatalytic performance.

According to the discussion above, the evolution of $TiO_2$/CdTe/BiOI heterostructures can be illustrated by Scheme 1. Alternatively, amorphous $TiO_2$ microspheres can also transform into $TiO_2$ solid microspheres directly via a simple calcination procedure. During the following hydrothermal process, the pre-existing $TiO_2$/CdTe QD microspheres could act as nucleation sites for BiOI crystallization, and thus, the ternary $TiO_2$/CdTe/BiOI heterostructures form simultaneously. It is well known that BiOI has an intrinsic rapid nucleation rate and growth rate; as a result, BiOI particles with relatively large size and few quantity form on the $TiO_2$(S), in a flake-like shape as growing along the [110] direction. However, in the case of $TiO_2$(H) microspheres, which possess larger surface for BiOI crystallization, BiOI particles tend to exist in a form which is relatively small in size and abundant in quantity. Therefore, the surface morphology of $TiO_2$ microspheres determines the shape and form of BiOI particles, as the SEM and TEM results suggested.

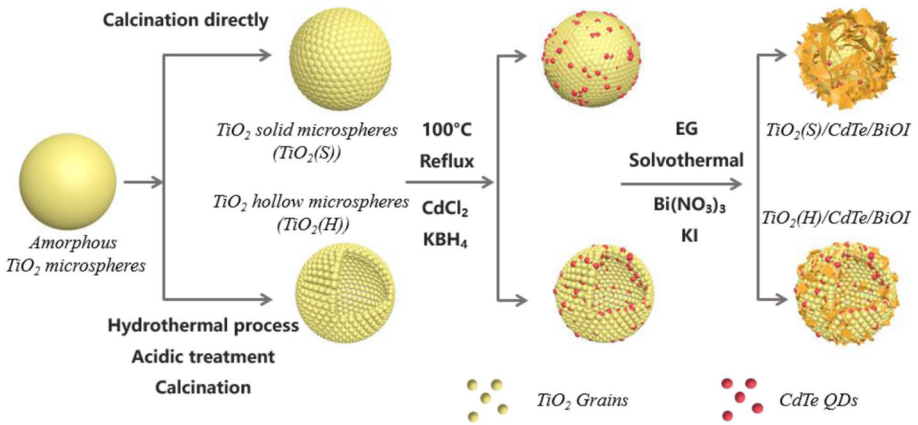


**Scheme 1** Structural evolution from amorphous $TiO_2$ to $TiO_2$/CdTe/BiOI heterostructures

XPS is employed to investigate the surface electronic states and the chemical composition of the as-prepared samples, and the results are shown in Fig. 5. It can be seen from the XPS survey spectrum that the $TiO_2$/CdTe/BiOI contains Ti, O, Bi, I, Cd, and Te elements. Figure 5b shows that the peaks in the high-resolution XPS spectrum of Ti 2p corresponding to binding energies of 458.5 eV and 464.2 eV are attributed to Ti $2p_{3/2}$ and Ti $2p_{1/2}$, which indicated a Ti(IV) oxidation state [26], and the measured binding energy (BE) separation of 5.7 eV is consistent with $TiO_2$ [27]. However, the binding energies of Ti $2p_{1/2}$ and Ti $2p_{3/2}$ for $TiO_2$/CdTe and $TiO_2$/CdTe/BiOI are 457.5 and 463.3 eV, respectively, both of which have a shift about 0.8 eV to the lower energy region compared with bare $TiO_2$, further proving a strong interaction between CdTe and $TiO_2$. The O 1 s core level spectrum (Fig. 5c) at around 529.5 eV is associated with the lattice O in the bare $TiO_2$ samples, which is related to Ti-O bonds [28]. It deserves to be mentioned that a shift towards the lower binding

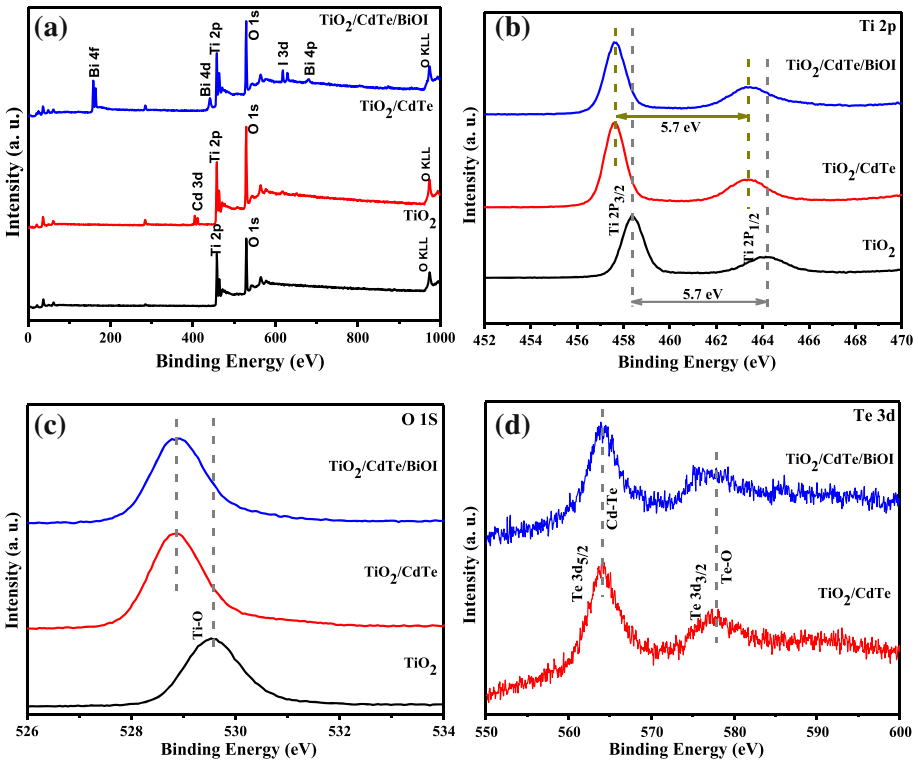


**Fig. 5 a** XPS scanning spectrum of the samples of $TiO_2$, $TiO_2$/CdTe, $TiO_2$/CdTe/BiOI. **b**–**d** High-resolution XPS spectra of Ti, O, and Te

energy of the O 1 s peak in the $TiO_2$/CdTe and $TiO_2$/CdTe/BiOI samples indicates loss of oxygen ions [27], which can be attributed to the partial oxidation of CdTe on $TiO_2$. This result fits well with the shift of Ti 2p and implies the formation of the interface among $TiO_2$, BiOI, and CdTe in heterojunction. The Te $3d_{5/2}$ spectra (Fig. 5e) reveal two states of tellurium at BE of 564.1 eV and 577.1 eV, respectively, which are characteristic for CdTe.

As the optical adsorption properties are supposed critical for the multi-component semiconductors, the optical absorption spectra of $TiO_2$(S), $TiO_2$(S)/CdTe, $TiO_2$(S)/BiOI, $TiO_2$(S)/CdTe/BiOI, and $TiO_2$(H)/CdTe/BiOI are shown in Fig. 6a. The as-prepared $TiO_2$ shows a similar trend as commercial P25, suggesting a typical ultraviolet response characteristic. As for the binary and ternary composites, the $TiO_2$(S)/CdTe/BiOI possesses a much more obvious absorption in the visible region than $TiO_2$(S)/CdTe and $TiO_2$(S)/BiOI, reflecting an enhanced

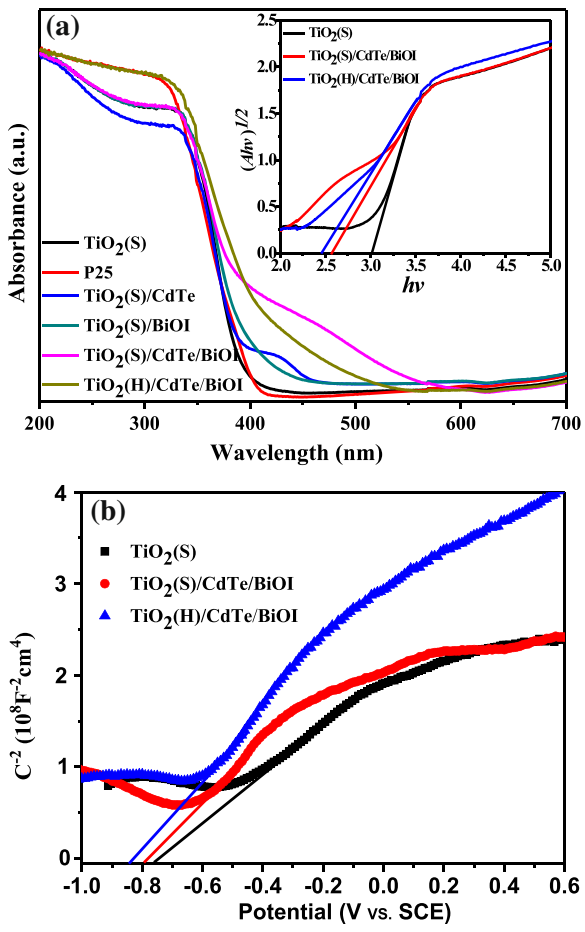


**Fig. 6 a** UV-Vis diffuse-reflectance spectra of all samples and corresponding Tauc plots of $TiO_2$(S), $TiO_2$(S)/CdTe/BiOI, and $TiO_2$(H)/CdTe/BiOI samples. **b** Mott-Schottky plots in 0.5 M $Na_2SO_4$ at a frequency of 1 KHz of $TiO_2$(S), $TiO_2$(S)/CdTe/BiOI, and $TiO_2$(H)/CdTe/BiOI samples

connection among the components by CdTe QD loading. And the absorption of $TiO_2$(S)/CdTe/BiOI in the visible range is a little weaker than that of $TiO_2$(H)/CdTe/BiOI; we attribute this phenomenon to the dispersive effect by hollow-structured $TiO_2$ microspheres as discussed above. The insert image shows the Tauc plots of $(Ahv)^{1/2}$ versus the $hv$ of samples. The bandgaps of $TiO_2$(S), $TiO_2$(S)/CdTe/BiOI, and $TiO_2$(H)/CdTe/BiOI are estimated by extrapolating the straight line to the abscissa axis and estimated to be 3.02 eV, 2.57 eV, and 2.45 eV, respectively. It is worth noting that $TiO_2$(S)/CdTe/BiOI displays a small bulge different from $TiO_2$(H)/CdTe/BiOI, regardless of the blue shift by 0.12 eV, suggesting nonuniform distribution of large BiOI particles as SEM results implied above.

In order to further comprehend the electronic properties and structure of both photocatalysts, the electrochemical Mott-Schottky experiment is performed in 0.5 M $Na_2SO_4$, as shown in Fig. 6b. From Fig. 6b, all samples show a positive slope in the Mott-Schottky plots, indicating that prepared composites are apparent n-type semiconductors [29, 30]. And the conduction band position (CB) energy of samples can be approximately equal to the flat-band potential ($E_{fb}$) via extrapolating the $X$ intercepts of the linear portion in the Mott-Schottky plots. The value of $E_{fb}$ of the $TiO_2$(S), $TiO_2$(S)/CdTe/BiOI, and $TiO_2$(H)/CdTe/BiOI is found to be − 0.76 V (vs SCE), − 0.80 V (vs SCE), and − 0.85 V (vs SCE), respectively. Since the SCE we used in the Mott-Schottky measurement possesses a value of − 0.24 V versus NHE [31], the CBM of $TiO_2$(S), $TiO_2$(S)/CdTe/BiOI, and $TiO_2$(H)/CdTe/BiOI samples could be calculated to be − 0.52 V (vs NHE), − 0.56 V (vs NHE), and − 0.6 V (vs NHE), respectively, which is more negative than the reduction potential of $O_2/{\bullet}O^-_2$ ($E^0(O_2/{\bullet}O^-_2)$ = − 0.33 V vs NHE). Furthermore, combined with the bandgap value from Fig. 6, the valence band maximum (VBM) is located at 2.5 V (vs NHE), 2.01 V (vs NHE), and 1.85 V (vs NHE), respectively.

Figure 7a shows the photocatalytic degradation of MO in solutions without catalyst and over different photocatalysts. It can be clearly seen that $TiO_2$ solid microspheres and P25 possess relatively poor photocatalytic activities under simulated sunlight, and the degradation is caused by the small ultraviolet portion from the light source. In contrast, the photocatalytic performance of $TiO_2$(S)/BiOI and $TiO_2$(S)/CdTe is slightly enhanced, and the MO removal percentage reached 46.3% and 57.5% after 180 min irradiation, respectively. It is worth noting that the photocatalytic degradation of MO could achieve 88.4% in 180 min and 99.7% in 90 min for $TiO_2$(S)/CdTe/BiOI and $TiO_2$(H)/CdTe/BiOI, respectively, due to synergistic binary visible-responding component BiOI and CdTe QDs. Furthermore, the more efficient $TiO_2$(H)/CdTe/BiOI over $TiO_2$(S)/CdTe/BiOI is

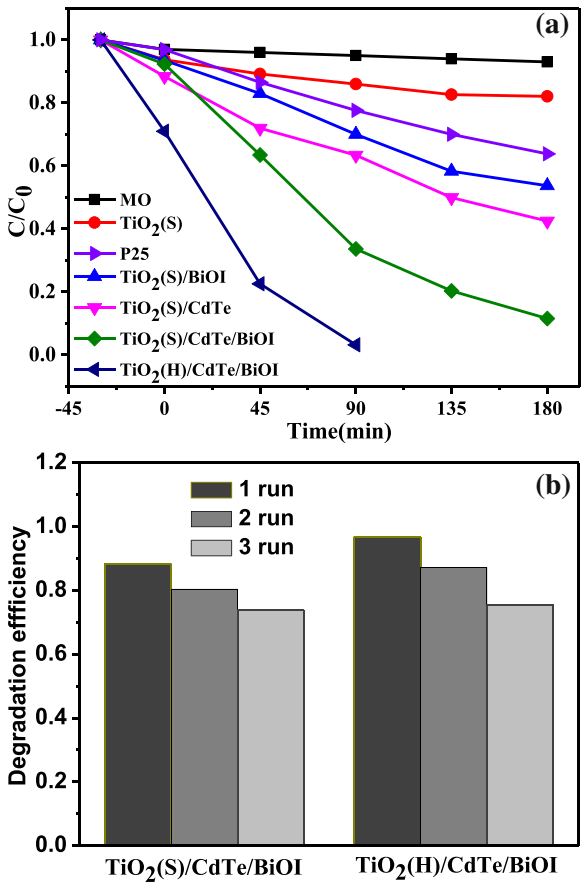


**Fig. 7** **a** Photocatalytic performance of the samples for MO removal. **b** Photocatalytic recycle experiments for the $TiO_2$(S)/CdTe/BiOI and $TiO_2$(H)/CdTe/BiOI samples

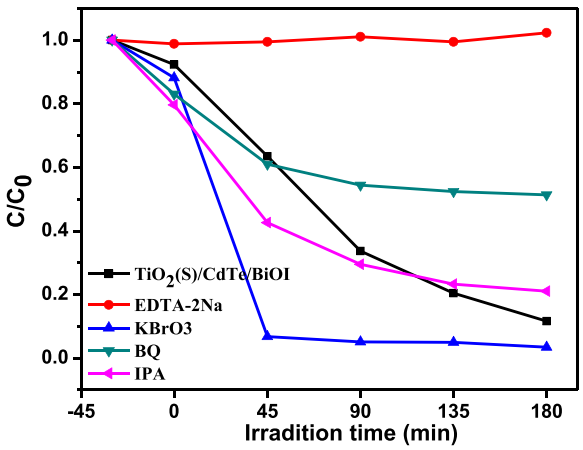


**Fig. 8** The plots of photodegraded performance of MO under trapping the different photogenerated active species of $TiO_2$(S)/CdTe/BiOI sample

probably caused by a slightly larger specific surface area (91.6 $m^2$ $g^{-1}$ over 77.7 $m^2g^{-1}$) as mentioned above. Figure 7b shows the cycle degradation experiment of $TiO_2$(S)/CdTe/BiOI and $TiO_2$(H)/CdTe/BiOI composites. There is a slight reduce of the photodegradation efficiency after three cycles.

In order to evaluate the pathway of the MO photocatalytic degradation by the $TiO_2$/CdTe/BiOI, the effect of $h^+$, $e^-$, •OH, and $•O^-_2$ was investigated by trapping experiment using EDTA-2Na ($h^+$), $KBrO_3$ ($e^-$), BQ ($•O^-_2$), and IPA (•OH). Figure 8 shows the degradation efficiency of MO during these photocatalytic experiments in the presence of the selected scavengers. It can be found that the photocatalytic process is suppressed than without any scavenger and the degradation efficiency is almost none in the presence of EDTA-2Na. However, the $e^-$ scavenger could accelerate the degradation, which demonstrated that the holes ($h^+$) are the main active species for the MO degradation. The BQ as $•O^-_2$ scavenger just influenced the degradation in a small degree, suggesting that $•O^-_2$ are partially responsible for the photocatalytic oxidation process. In addition, the influence of IPA on the $TiO_2$/CdTe/BiOI sample removing MO is hardly observed, indicating that •OH radicals are hardly useful in the current photocatalytic system.

The photoluminescence emission spectroscopy (PL) is conducted to further study the transfer behavior of photogenerated charge carriers. As shown in Fig. 9, all samples show a broad PL emission peak at about 450–500 nm with the excitation at 365 nm. The bare $TiO_2$(S) has a strong emission peak, while $TiO_2$(S)/CdTe/BiOI sample displays lower intensity than that of $TiO_2$(S). This phenomenon indicates that the recombination rate of photogenerated charge carriers was efficiently restrained after decorating CdTe and BiOI on the surface of $TiO_2$. Furthermore, the $TiO_2$(H)/CdTe /BiOI exhibits significantly diminished PL intensity in

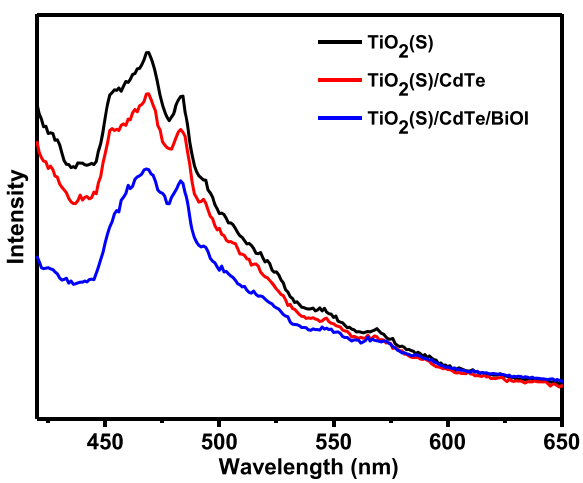


**Fig. 9** Photoluminescence spectra of the bare $TiO_2$(S), $TiO_2$(S)/CdTe/BiOI, and $TiO_2$(H)/CdTe/BiOI samples ($\lambda$ excitation = 365 nm)

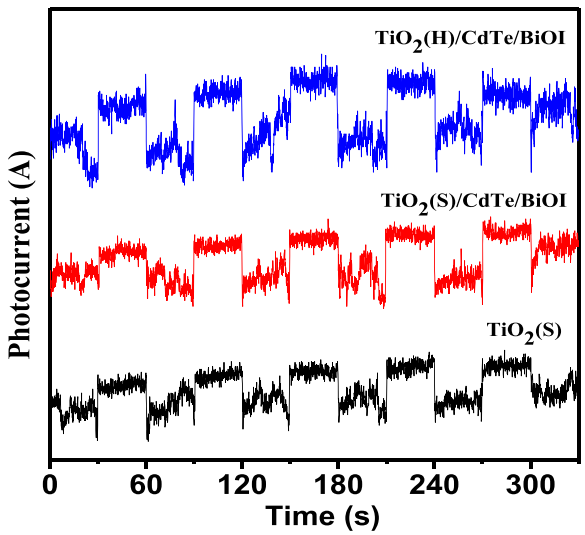


**Fig. 10** The transient photocurrent response of $TiO_2$(S), $TiO_2$(S)/CdTe/BiOI, and $TiO_2$(H)/CdTe/BiOI

comparison with the other samples, which is cause by the faster transfer of electrons and holes from CdTe QDs or BiOI nanosheets to the surface of $TiO_2$. The PL results are consistent with the result from photodegradation experiment.

The photocurrent of samples is shown in Fig. 10. It was worth noting that the $TiO_2$(S)/CdTe composites exhibited higher photocurrent response than that of pure $TiO_2$(S) and $TiO_2$(S)/CdTe/BiOI composites. Therefore, the increased photocurrent could be mainly attributed to the efficient photogenerated separation and migration, which benefits for the photocatalytic performance.

Based on the results and discussions above, we propose a synergistic CdTe QDs/BiOI sensitization mechanism of the exciton transfer in $TiO_2$/CdTe/BiOI to explain the enhanced photo activity, as illustrated in Scheme 2. It is well known that $TiO_2$ with a wide bandgap (3.02 eV) could only utilize the UV region in solar light, while the narrow bandgap CdTe QDs (~ 1.5 eV) [32] and BiOI nanostructures (~ 1.8 eV) [33] can be excited by photons in the visible range. In addition, a p-n junction is formed between p-type BiOI and n-type $TiO_2$ when Fermi levels reached equilibrium, which facilitate photo-induced electrons to migrate from CB of BiOI to that of $TiO_2$ [17, 34]. Similarly, a type II heterojunction is formed between p-type CdTe [18] and $TiO_2$ microspheres; thus, electrons in the CB of CdTe QDs can transfer to $TiO_2$ [35]. Therefore, the lifetime of the photogenerated electron and hole is prolonged, which is beneficial for the degradation towards MO.

## Conclusions

In summary, a series of $TiO_2$-based photocatalysts were synthesized by a facile hydrothermal method. Modifications by BiOI and CdTe QDs were carried out to fabricate binary and ternary heterostructures, and the narrow bandgap semiconductors extended light response for the hybrid photocatalysts. In the case of ternary $TiO_2$/CdTe/BiOI heterostructured photocatalyst, the BiOI flakes and CdTe QDs act as sensitizers on one hand, which are excited by simulated solar light and transfer electrons to $TiO_2$. Meanwhile, the $TiO_2$ microspheres serve as separation centers for the photo-induced charges on the other hand; thus, the synergistic effect among $TiO_2$, CdTe, and BiOI enhances the photocatalytic removal of MO. In addition, hollow $TiO_2$ precursors were also employed

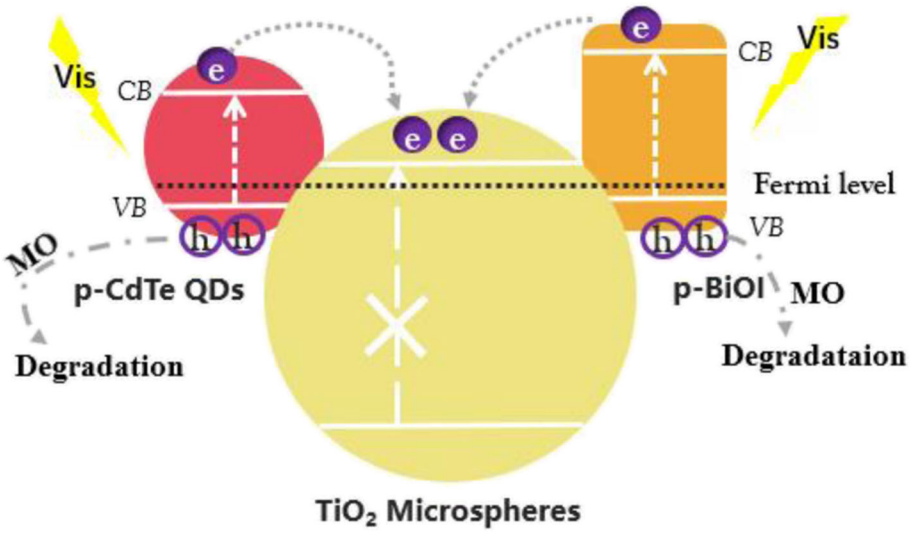


**Scheme 2** Illustration of photo-induced charge transfer in ternary $TiO_2$/CdTe/BiOI photocatalytic system

to fabricate $TiO_2$/CdTe/BiOI heterostructures, and the improved photocatalytic performance towards MO degradation is attributed to a higher surface area and dispersion of BiOI components. The strategy of material regulation and incorporation will provide possibilities for the design of the multi-component semiconductor photocatalysts.

#### Abbreviations

$TiO_2$(H): $TiO_2$ hollow microspheres; $TiO_2$(S): $TiO_2$ solid microspheres; $TiO_2$/BiOI: $TiO_2$ spheres modified with BiOI; $TiO_2$/CdTe: $TiO_2$ spheres modified with CdTe QDs; $TiO_2$/CdTe/BiOI: $TiO_2$, CdTe, and BiOI ternary composites

#### Acknowledgements

Not applicable.

#### Funding

This work was mainly funded by the Nation Natural Science Foundation of China (NSFC, Grant No. 61504073) and A Project of Shandong Province Higher Educational Science and Technology Program (No. J18KA011).

#### Availability of Data and Materials

Data sharing is not applicable to this article as no datasets were generated or analysed during the current study.

#### Authors' Contributions

XF and SL conceived and designed the experiments and were major contributors in performing the analysis with constructive discussions. MH, LF, and CH performed the experiments and analyzed the data. CQ and MH wrote the manuscript. JH and FL contributed the materials and analysis tools. All authors read and approved the final manuscript.

#### Competing Interests

The authors declare that they have no competing interests.

## Publisher's Note



#### Author details

[1]College of Materials Science and Engineering, Qingdao University of Science and Technology, Zhengzhou Road 53, Qingdao 266042, China. [2]Ansteel Cold Rolling (PuTian) Co., Ltd., Wangshan East Road 555, Putian 351100, China.

Received: 17 October 2018 Accepted: 27 January 2019
Published online: 06 February 2019

#### References

1. Zhong WW, Tu WG, Xu Y, Zhan BS, Jin SF, Xu R (2017) Conductive FeSe nanorods: a novel and efficientco-catalyst deposited on $BiVO_4$, for enhanced photocatalytic activity under visible light. J Environ Chem Eng 5:4206–4211
2. Zhong WW, Tu WG, Feng SS, Xu AJ (2019) Photocatalytic $H_2$ evolution on CdS nanoparticles by loading FeSe nanorods as co-catalyst under visible light irradiation. J Alloys Compd 772:669–674
3. Liu X, Chen Z, Li W, Cao M (2017) Distinctly improved photocurrent and stability in $TiO_2$ nanotube arrays by ladder band structure. J Phys Chem C 121:20605–20612
4. Vequizo JJM, Matsunaga H, Ishiku T, Kamimura S, Ohno T, Yamakata A (2017) Trapping-induced enhancement of photocatalytic activity on brookite $TiO_2$ powders: comparison with anatase and rutile $TiO_2$ powders. ACS Catal 7(4):2644–2651
5. Magdziarz A, Colmenares JC, Chernyayeva O, Lisovytskiy D, Grzonka J, Kurzydłowski K, Freindl K, Korecki J (2017) Insight into the synthesis procedure of $Fe^{3+}$/$TiO_2$-based photocatalyst applied in the selective photo-oxidation of benzyl alcohol under sun-imitating lamp. Ultrason Sonochem 38:189–196
6. Liu B, Jiang Y, Wang Y, Shang SX, Ni YM, Zhang N, Cao MH, Hu CW (2018) Influence of dimensionality and crystallization on visible-light hydrogen production of Au@$TiO_2$ core-shell photocatalysts based on localized surface plasmon resonance. Catal Sci Technol 8:1094–1103
7. Zhang J, Zhang LL, Shi YX, Xu GL, Zhang EP, Wang HB, Kong Z, Xi JH, Ji ZG (2017) Anatase $TiO_2$ nanosheets with coexposed {101} and {001} facets coupled with ultrathin $SnS_2$ nanosheets as a face-to-face n-p-n dual heterojunction photocatalyst for enhancing photocatalytic activity. Appl Surf Sci 420:839–848
8. Chen PP, Cai YY, Wang J, Wang KW, Tao YS, Xue JD, Wang HG (2018) Preparation of protonized titanate nanotubes/$Fe_3O_4$/$TiO_2$ ternary composites and dye self-sensitization for visible-light-driven photodegradation of Rhodamine B. Powder Technol 326:272–280
9. Chen F, Yang Q, Wang YL, Zhao JW, Wang DB, Li XM, Guo Z, Wang H, Deng YC, Niu CG, Zeng GM (2017) Novel ternary heterojunction photcocatalyst of ag nanoparticles and g-$C_3N_4$, nanosheets co-modified $BiVO_4$ for wider spectrum visible-light photocatalytic degradation of refractory pollutant. App Catal B Environ 205:133–147
10. Zhu Y, Shah MW, Wang C (2017) Insight into the role of $Ti^{3+}$ in photocatalytic performance of shuriken-shaped $BiVO_4$/$TiO_{2-x}$ heterojunction. App Catal B Environ 203:526–532
11. Di J, Xia JX, Ji MX, Yin S, Li HP, Xu H, Zhang Q, Li HM (2015) Controllable synthesis of $Bi_4O_5Br_2$ ultrathin nanosheets for photocatalytic removal of ciprofloxacin and mechanism insight. J Mater Chem A 3(29):15108–15118
12. Bhachu DS, Moniz SJA, Sathasivam S, Scanlon DO, Walsh A, Bawaked SM, Mohamed M, Obaid AY, Parkin IP, Tang JW, Carmalt CJ (2016) Bismuth oxyhalides: synthesis, structure and photoelectrochemical activity. Chem Sci 7(8):4832–4841
13. Ye KH, Chai ZS, Gu JW, Yu X, Zhao CX, Zhang YM, Mai WJ (2015) BiOI-$BiVO_4$, photoanodes with significantly improved solar water splitting capability: p-n junction to expand solar adsorption range and facilitate charge carrier dynamics. Nano Energy 18:222–231
14. Peng JH, Zhao YJ, Hassan QU, Li HY, Liu YB, Ma SH, Mao DL, Li HQ, Meng LC, Hojamberdiev M (2018) Rapid microwave-assisted solvothermal synthesis and visible-light-induced photocatalytic activity of $Er^{3+}$-doped BiOI nanosheets. Adv Powder Technol 29(5):1158–1166
15. Peng Y, Liu T, Xu J, Wang KK, Mao YG (2017) Facet-selective interface design of a $BiOI_{(110)}$/Br-$Bi_2O_2CO_{3(110)}$ p–n heterojunction photocatalyst. Crystengcomm 19(45):6837–6844
16. Buchholcz B, Haspel H, Oszkó A, Kukovecz A, Kónya Z (2017) Titania nanotube stabilized BiOCl nanoparticles in visible-light photocatalysis. RSC Adv 7(27):16410–16422
17. Liu J, Ruan L, Adeloju SB, Wu Y (2014) BiOI/$TiO_2$ nanotube arrays, a unique flake-tube structured p-n junction with remarkable visible-light photoelectrocatalytic performance and stability. Dalton Trans 43(4):1706–1715
18. Han GP, Wang WN, Liu B, Pei CJ, Zhao H, Liu JF, Yang HP (2017) Visible-light photocatalysis in CdTe nanoflakes with exposed {111} facets and charge separation between polar CdTe {111} surfaces. App Catal B Environ 208:94–103
19. Bajorowicz B, Nadolna J, Lisowski W, Klimczuk T, Zaleska-Medynska A (2017) The effects of bifunctional linker and reflux time on the surface properties and photocatalytic activity of CdTe quantum dots decorated $KTaO_3$, composite photocatalysts. App Catal B Environ 203:452–464
20. Feng H, Thanhthuy TT, Chen L, Yuan L, Cai Q (2013) Visible light-induced efficiently oxidative decomposition of p-Nitrophenol by CdTe/$TiO_2$ nanotube arrays. Chem Eng J 215-216:591–599
21. Liu Y, Chen F, Li Q (2018) Synthesis of CdTe/carbon nanotube/ZnO flower-like micro-spheres and their photocatalytic activities in degradation of rohdamine B. Mater Lett 210:23–25
22. Zhou WQ, Yu CL, Fan QZ, Wei LF, Chen JC, Yu JC (2013) Ultrasonic fabrication of N-doped $TiO_2$ nanocrystals with mesoporous structure and enhanced visible light photocatalytic activity. Chin J Catal 34(6):1250–1255
23. Yu C, Yu JC, Fan C, Wen H, Hu S (2010) Synthesis and characterization of Pt/BiOI nanoplate catalyst with enhanced activity under visible light irradiation. Mater Sci Eng B 166(3):213–219
24. Sing KSW (1985) Reporting physisorption data for gas/solid systems-with special reference to the determination of surface area and porosity. Pure & Applied Chemistry 57(4):603–619
25. Li JQ, Wang DF, Liu H, Du J, Zhu ZF (2012) Nanosheet-based $BiVO_4$ hierarchical microspheres and their photocatalytic activity under visible light. Phys Status Solidi 209(2):248–253
26. Li JZ, Zhong JB, Si YJ, Huang ST, Dou L, Li MJ, Liu YP, Ding J (2016) Improved solar-driven photocatalytic performance of BiOI decorated $TiO_2$

benefiting from the separation properties of photo-induced charge carriers. Solid State Sci 52:106–111
27. Shinde PS, Park JW, Mahadik MA, Ryu J, Park JH, Yi YJ, Jang JS (2016) Fabrication of efficient CdS nanoflowers-decorated $TiO_2$ nanotubes array heterojunction photoanode by a novel synthetic approach for solar hydrogen production. Int J Hydrog Energy 41(46):21078–21087
28. Lu DZ, Fang PF, Wu WH, Ding JQ, Jiang LL, Zhao XN, Li CH, Yang MC, Li YZ, Wang DH (2017) Solvothermal-assisted synthesis of self-assembling $TiO_2$ nanorods on large graphitic carbon nitride sheets with their anti-recombination in the photocatalytic removal of Cr(vi) and rhodamine B under visible light irradiation. Nanoscale 9:3231–3245
29. Martin DJ, Reardon PJT, Moniz SJA, Tang JW (2014) Visible light-driven pure water splitting by a nature-inspired organic semiconductor-based system. J Am Chem Soc 136(36):12568–12571
30. Hsu YK, Yu CH, Chen YC, Lin YG (2013) Synthesis of novel $Cu_2O$ micro/nanostructural photocathode for solar water splitting. Electrochim Acta 105:62–68
31. Patil SS, Tarwal NL, Yadav HM, Korade SD, Bhat TS, Teli AM, Karanjkar MM, Kim JH, Patil PS (2018) Photoelectrochemical performance of dye and semiconductor sensitization on 1-D hollow hexagonal ZnO rods: a comparative study. J Solid State Electrochem 22:3015–3024
32. Feng H, Tang N, Zhang S, Liu B, Cai Q (2017) Fabrication of layered (CdS-Mn/$MoS_2$/CdTe)-promoted $TiO_2$ nanotube arrays with superior photocatalytic properties. J Colloid Interface Sci 486:58–66
33. Yosefi L, Haghighi M (2018) Fabrication of nanostructured flowerlike p-BiOI/p-NiO heterostructure and its efficient photocatalytic performance in water treatment under visible-light irradiation. App Catal B Environ 220:367–378
34. Zhang Y, Pei Q, Liang JC, Feng T, Zhou X, Mao H, Zhang W, Hisaeda Y, Song XM (2015) Mesoporous $TiO_2$-based photoanode sensitized by BiOI and investigation of its photovoltaic behavior. Langmuir Acs J Surf Colloids 31(37):10279
35. Ai GJ, Mo R, Xu H, Chen Q, Yang S, Li HX, Zhong JX (2015) Vertically aligned $TiO_2$/(CdS, CdTe, CdSTe) core/shell nanowire array for photoelectrochemical hydrogen generation. J Power Sources 280(4):5–11